



Coiled-tube heat exchanger for high-pressure metal hydride hydrogen storage systems – Part 2. Computational model

Milan Visaria, Issam Mudawar*

Hydrogen Systems Laboratory (HSL) and Boiling and Two-Phase Flow Laboratory (BTPFL), School of Mechanical Engineering, Purdue University, West Lafayette, IN 47907, United States

ARTICLE INFO

Article history:

Available online 13 December 2011

Keywords:

Fuel cells
Hydrogen storage
Heat exchangers

ABSTRACT

This second part of a two-part study presents a transient, three-dimensional numerical model for a high-pressure metal hydride (HPMH) hydrogen storage system that is cooled by a coiled-tube heat exchanger. The model uses the same geometry examined in the first part of the study and its predictions are compared to experimental results also discussed in the first part. The model involves solving coupled heat diffusion and hydriding reaction equations for $Ti_{1.1}CrMn$. These equations are solved to determine the spatial distribution of hydride temperature as a function of time over the entire duration of the hydriding reaction, which is shown to agree favorably with the experimental data. The model also serves as an effective means for tracking the detailed temporal variations of the heat exchanger's key performance parameters for different hydride locations relative to the coolant tube. These variations can aid in determining optimum placement of the coolant tube relative the hydride powder. Like the experimental study, the model proves that coolant temperature has the greatest influence on the time needed to complete the hydriding reaction.

© 2011 Elsevier Ltd. All rights reserved.

1. Introduction

Because of hydrogen's very low density, storing an adequate amount of hydrogen onboard an automobile for fuel cell use is quite an elusive task. One of several storage methods being proposed is by reaction with a high-pressure metal hydride (HPMH) such as $Ti_{1.1}CrMn$ instead of very high pressure gas or very low temperature liquid [1–4]. One of the primary challenges in the development of a hydrogen storage system utilizing HPMH is the ability to safely and effectively remove the large amount of heat released once the hydrogen is charged into the automobile at the filling station. This challenge renders the heat exchanger the most crucial component of such a storage system. The heat exchanger must meet two important design requirements: (a) removing the heat in a short duration called fill time, and (b) minimizing the volume of the heat exchanger components to maximize the space available in the storage pressure vessel for the HPMH and, therefore, the hydrogen itself.

The first part of this two-part study [5] showed how these two design requirements are difficult to accomplish simultaneously. A simple, coiled-tube heat exchanger was developed and tested to

assess its performance subject to different operating conditions. This design was shown to provide very high storage capacity, albeit at the expense of a longer fill time. This second part of the study will provide a 3-D computational model to predict the transient cooling performance of the heat exchanger.

Storage of hydrogen using HPMHs involves a reversible chemical reaction (chemisorption) between hydrogen atoms and metal hydride particles. When the hydrogen is charged into the storage pressure vessel, an exothermic 'hydriding' reaction takes place, where a large amount of heat is dissipated and must be removed by the heat exchanger. A reverse endothermic 'dehydriding' reaction occurs when the hydride is heated to release the hydrogen to the fuel cell. Here, the heat exchanger is used to heat the hydride to achieve the hydrogen release. The present study concerns the hydriding reaction.

As discussed in this paper, the hydriding reaction is (i) self-limiting (reaction rate decreases as the reaction progresses), (ii) kinetically-driven (reaction rate depends on the hydride's kinetic parameters such as activation energy, heat of reaction, and equilibrium pressure), and (iii) thermally limited (reaction rate is inversely proportional to the hydride temperature). Because of the latter, the hydriding process depends not only on the intrinsic properties of the metal hydride, but also on externally-controlled parameters like temperature and pressure, which explains why the heat exchanger is such a crucial component of the storage system.

* Corresponding author. Tel.: +1 765 494 5705; fax: +1 765 494 0539.

E-mail address: mudawar@ecn.purdue.edu (I. Mudawar).

URL: <https://engineering.purdue.edu/BTPFL> (I. Mudawar).

where C_a , E_a , R and P_{eq} are the hydriding constant, activation energy, universal gas constant, and equilibrium pressure, respectively. Eq. (3) shows that the reaction rate is self-limiting, i.e., at a given temperature and pressure, the rate of reaction (dF/dt) decreases as the reaction progresses (as F increases) and is zero when the reaction reaches completion ($F = 1$). It is assumed that the metal hydride is initially completely dehydrided, i.e., $F = 0$. From Eq. (3), it can be seen that, apart from the hydride properties, the reaction rate depends on the metal hydride temperature, T , system pressure, P , and equilibrium pressure, P_{eq} . The equilibrium pressure is obtained from the van't Hoff equation [14],

$$P_{eq} = P_o \exp\left(\frac{\Delta H_r}{RT} - \frac{\Delta S}{R}\right), \quad (4)$$

where P_o and ΔS are atmospheric pressure and entropy of reaction, respectively.

Starting with the initial metal hydride temperature, P_{eq} and reaction rate, dF/dt , are computed using Eq. (4) and Eq. (3), respectively. The heat generation rate, \dot{q}''' , is then computed using Eq. (2) and introduced into Eq. (1) to solve for the hydride temperature distribution after the next time step. The computation is repeated and the transient profiles of metal hydride temperature, reaction progress, and heat generation rate are all calculated until the reaction reaches completion ($F = 1$). Notice from Eqs. (3) and (4), that, to increase reaction rate, either the system pressure must be increased or equilibrium pressure decreased by lowering the hydride temperature.

In the present analysis, it is assumed that the hydrogen behaves as an ideal gas. At any instant during the hydriding reaction, the amount of hydrogen per unit volume is the sum of the hydrogen absorbed by the metal hydride, F (wt%) ρ_{MH} , and hydrogen in the gas phase (calculated from the ideal gas equation) within the pores of the hydride. Pressure inside the vessel is assumed time dependent but spatially uniform. Due to the relatively low temperatures (less than 55 °C) associated with hydriding reaction, radiation heat transfer effects are neglected.

2.2. Thermal and kinetic properties

To compare the model predictions with experimental data, it is important that correct thermal and kinetic properties of the metal hydride be used. Measuring the properties of $Ti_{1.1}CrMn$ is a challenging task due to the following reasons:

1. Activated $Ti_{1.1}CrMn$ used for hydrogen storage is in powder form with particle size below 10 μm .
2. $Ti_{1.1}CrMn$ spontaneously ignites in the presence of air or moisture and, hence, its handling is both difficult and dangerous.
3. Properties must be measured at high pressures (up to 300 bar) of interest to hydrogen storage.
4. Properties depend on many parameters such as pressure, temperature, reaction progress, particle size, number of cycles, etc.

Because of these factors and limited number of studies on $Ti_{1.1}CrMn$, its properties, especially at high pressures, are not readily available. Therefore, the thermal properties of this hydride, such as k_{MH} and $c_{p,MH}$, as well as its kinetic properties, such as wt%, ΔH_r and ΔS , had to be measured experimentally at the Purdue University Hydrogen Systems Laboratory (HSL).

2.3. Effective thermal conductivity (k_{MH})

Thermal properties of $Ti_{1.1}CrMn$ were measured using the Transient Plane Source (TPS) technique. TPS uses a resistive element that serves both a heat source and temperature sensor. The resis-

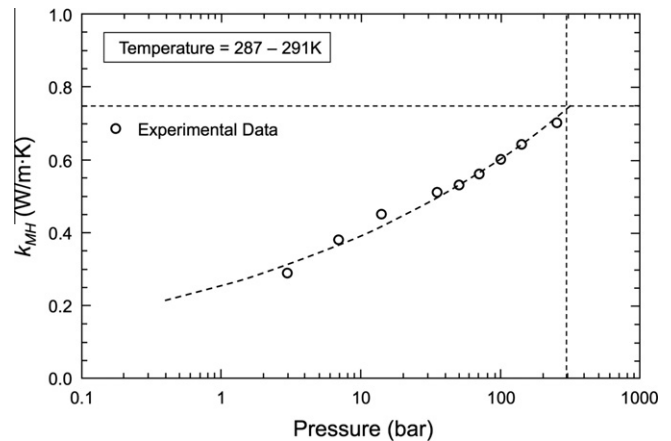


Fig. 1. Variation of effective thermal conductivity of $Ti_{1.1}CrMn$ with pressure.

tive element is sandwiched between two identical metal hydride samples. When a small current is passed through the resistive element, the temperatures of the hydride samples and the sensor begin to increase. The temperature response of the sensor is correlated to the thermal conductivity and thermal diffusivity of the hydride. A detailed description of the construction and measurement procedure of the TPS used in the present study is given in [15].

The $Ti_{1.1}CrMn$ measurements were made in a sealed pressure vessel filled with hydrogen gas at pressures ranging from 2.8 to 253 bar and temperatures between 14 and 18 °C. Fig. 1 shows the effective thermal conductivity of $Ti_{1.1}CrMn$ steadily increases from 0.3 W/m K at 2.8 bar to 0.71 W/m K at 253 bar [15]. This increase with pressure is attributed to more hydrogen atoms filling the interstitial gaps in the hydride powder.

Although k_{MH} increases with pressure, a mean constant value is used in the model. Since the peak pressure during the present experiments (280 bar) is higher than the maximum pressure at which k_{MH} was measured (253 bar), a slightly higher value of 0.75 W/m K is used. Using a constant k_{MH} of 0.75 W/m K in the model is justified by the fact that, in the present experiments, the pressure was increased during the hydriding reaction from 70 to 280 bar within 60 s (300 s during one test). Thereafter, the pressure was maintained at 280 bar through the remainder of hydriding reaction (greater part of the hydriding period). Use of constant properties both simplifies the model and allows for faster convergence.

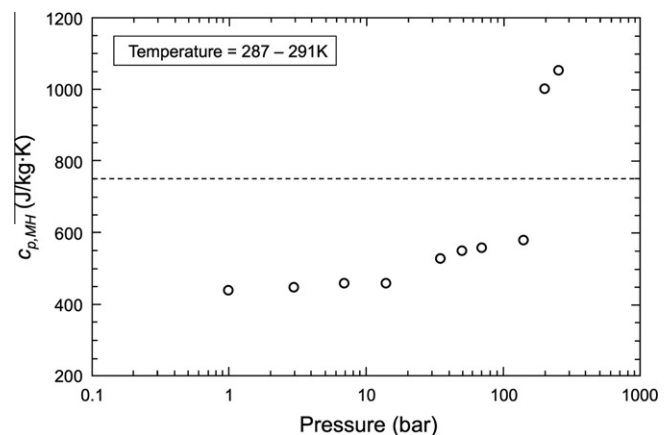


Fig. 2. Variation of specific heat capacity of $Ti_{1.1}CrMn$ with pressure.

2.4. Specific heat ($c_{p,MH}$)

By directly measuring the thermal conductivity, k_{MH} , and thermal diffusivity, α_{MH} , and knowing the density of $Ti_{1.1}CrMn$ samples used in the TPS system, Flueckiger et al. [15] were able to calculate its specific heat, $c_{p,MH}$. Fig. 2 shows the resulting variation of $c_{p,MH}$ with pressure. Before the hydriding phase (below 170 bar), $c_{p,MH}$ does not show a significant dependence on pressure, increasing from about 400 J/kg K at 1 bar to 580 J/kg K at 170 bar. However, above 170 bar, $c_{p,MH}$ suddenly increases to 1000 J/kg K. This behavior is attributed to the change in metal hydride lattice structure in response to the hydriding reaction. Flueckiger et al. also showed that $c_{p,MH}$ increases from 400 J/kg K at zero reaction progress ($F=0$) to 700 J/kg K at $F=0.7$. Thereafter, an abrupt jump to 1000 J/kg K was observed. It can therefore be concluded that $c_{p,MH}$ is a function of both and pressure and reaction progress.

In the present coiled-heat exchanger study, the pressure was increased quickly (in 60 s for three test, 300 s for one test) to 280 bar [5]. As a result of this short pressurization ramp, the reaction progress, F , of the metal hydride particles ranged between 0 and 1 (depending on location and temperature), even when the pressure was already 280 bar. Therefore, depending on the pressure and the state of hydriding, the specific heat of metal hydride particles could range from 400 to 1000 J/kg K. Since the model cannot handle such a broad range of $c_{p,MH}$ values across the metal hydride bed at each time step, or the sudden jump in $c_{p,MH}$ values during the hydriding phase, a constant average value of $c_{p,MH} = 750$ J/kg K is assumed.

2.5. Other kinetic and thermal properties

The hydrogen storage capacity, wt%, of the metal hydride is very sensitive to impurities. For this reason, even when the same metal hydride sample used in different storage vessels, its capacity must be re-measured before each new fill. This also helps account for any possible contamination during storage. Using the Sievert apparatus [16], a hydrogen storage capacity of $Ti_{1.1}CrMn$ of wt% = 1.3 was measured at 280 bar. The Sievert apparatus was also used to measure the enthalpy of reaction, ΔH_r , and entropy of reaction, ΔS , of $Ti_{1.1}CrMn$ [3,16]. The value of activation rate, C_a , is based on previous experiments conducted by the authors [3], while that of activation energy, E_a , is estimated from $LaNi_5$ measurements by Suda et al. [7]. Table 1 provides a summary of all the properties of $Ti_{1.1}CrMn$ used in the model. Additional details of these properties are available in [3].

2.6. Computation domain

In the experiments, the hydride temperature is measured only along the coiled section of the coolant tube. Hence, the model presented here examines the portion of the storage vessel containing the coiled section. Coil symmetry facilitates simplifying the model by using a representative portion of the coiled section instead of

the entire vessel. Fig. 3 shows the computational domain of the model created in Fluent. This hydride domain is bounded on the outside by the inner boundary of the containment vessel that houses the metal hydride and coiled-tube. To reduce the number of computation elements, the coolant tube is modeled as a hollow tube, with its wall thickness (1.65 mm) incorporated into an equivalent resistance that is applied to the tube surface. While symmetry requires using a domain length equal to only half the coil pitch, the model uses a domain length one-and-a-half times the coil pitch to ensure that key thermocouple locations in the experiments are precisely reproduced in the model.

2.7. Initial conditions

The model is intended to compare predictions with experimental data starting from the onset of the pressurization ramp (70 to 280 bar) until the metal hydride is completely hydrided. Hence, the initial pressure is set at 70 bar. It is also assumed that the metal hydride is initially in completely dehydrided state ($F=0$). This assumption is justified by the fact that the hydride's equilibrium pressure at 0 °C is 105 bar and hydriding cannot commence with an initial pressure below the equilibrium value. Additionally, the equilibrium pressure and, hence, the pressure required to initiate the hydriding increases with increasing temperature. The initial temperature of the metal hydride is set equal to the average of the temperatures measured experimentally at the onset of the pressurization ramp by the thermocouples embedded in the metal hydride powder.

2.8. Boundary conditions

As shown in Fig. 3, the boundary faces along the axial direction are assumed adiabatic due to symmetry. During the experiments, the outer doors of the test cell, where the experiments were conducted, were kept open as a safety measure. Lower temperature of the ambient air (0 to 5 °C) compared to the contents of the pressure vessel causes some heat to be lost by free convection. This heat loss was calculated based on the ambient air temperature and dimensions of the pressure vessel. An effective heat transfer coefficient, which accounts for both free convection and conduction resistance across the 44.45-mm (1.75-in) thick pressure vessel walls, is also applied to the circular face of the containment vessel. Heat transfer along the surface of the coiled tube is determined with the aid of an equivalent resistance that accounts for contact resistance, R_{tc} , between the hydride powder and tube surface, conductive resistance across the tube wall, and convective resistance inside the tube. This allows the boundary condition to be represented by the coolant's temperature and an effective heat transfer coefficient, h_{eff} , given by

$$\frac{1}{h_{eff}} = \frac{r_2}{r_1} \frac{1}{h_i} + \frac{r_2}{k_{ss}} \ln\left(\frac{r_2}{r_1}\right) + R_{tc}. \quad (5)$$

The internal convective heat transfer coefficient, h_i , in Eq. (5) is determined from the coolant's flow rate. The contact resistance is estimated at $R_{tc} = 2000$ mm² K/W based on previous experiment studies [3,15]. The coolant temperature is set equal to the value measured experimentally.

3. Comparison of model predictions with experimental data

The coiled-tube heat exchanger was tested under four different sets of operating conditions given in Table 2. The experimental results from these tests were discussed in details in part 1 [5]. Tests 1, 2 and 3 were conducted with the same pressurization rate of 70 to 280 bar in 60 s, while the same pressure increase was applied in

Table 1
Metal hydride properties used in model.

<i>Kinetic properties</i>	
Activation energy	$E_a = 20.7$ kJ/mol- H_2
Activation rate	$C_a = 150$ s ⁻¹
Enthalpy of reaction	$\Delta H_r = -14,390$ J/mol- H_2
Entropy of reaction	$\Delta S = -91.3$ J/mol- H_2
H_2 storage capacity	1.3 wt%
<i>Thermal properties</i>	
Packing density	$\rho_{MH} = 2200$ kg/m ³
Effective thermal conductivity	$k_{MH} = 0.75$ W/m K
Specific heat	$c_{p,MH} = 750$ J/kg K
Contact resistance	$R_{tc} = 2000$ mm ² K/W

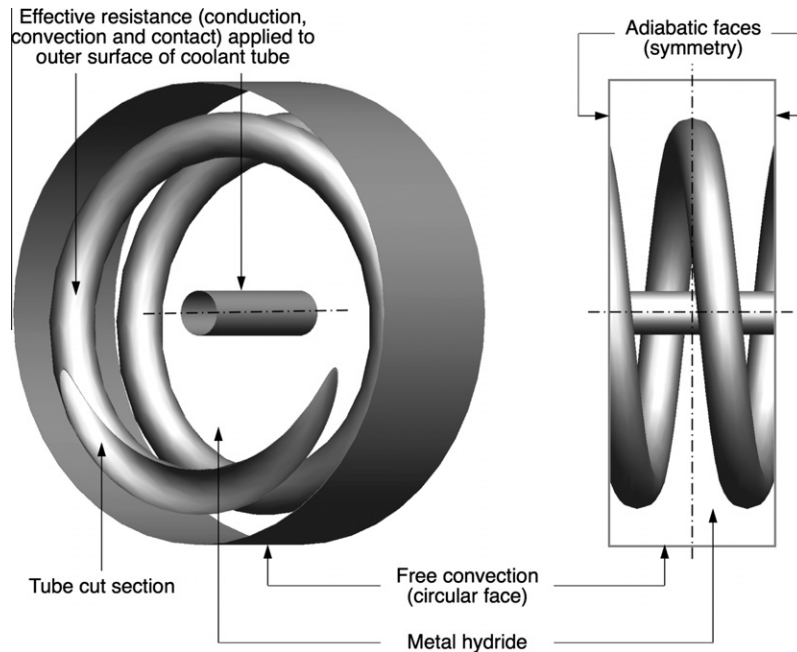


Fig. 3. Metal hydride domain of computational model.

Table 2
Operating parameters for tests performed.

Test no.	Pressurization profile	Coolant flow rate	Coolant temp. (°C)	Avg. initial temp. (°C)
1	70 to 280 bar in 60 s	11.5 lpm	2.5	4.5
2	70 to 280 bar in 60 s	14.2 lpm	21.0	20
3	70 to 280 bar in 60 s	No coolant flow		17
4	70 to 280 bar in 300 s	12.0 lpm	4.5	5.5

test 4 over 300 s. Test 1 had the lowest coolant temperature (2.5 °C) and test 2 the highest (21 °C). In test 3, the chiller was turned off so no coolant was supplied through the coiled tube, which is equivalent to having a storage system without a heat exchanger. In the absence of coolant flow in test 3, heat dissipated by

the hydride powder was rejected very slowly by free convection and conduction through the containment and pressure vessel walls and cover plates. Because of the difficulty in accurately quantifying those heat flow modes, the present model is applied to tests 1, 2 and 4 but not 3.

As explained in part 1 [5], the metal hydride temperature was measured as 13 locations within the powder, four of which adequately represent the spatial response of the entire hydride bed. Figs. 4–6 compare the model predictions of hydride temperature profiles for those four locations to the measured response for tests 1, 2 and 4, respectively. Locations 1 to 4 in each figure are detailed in part 1 and correspond to increasing distances from the coolant tube. Overall, there is good agreement between the predicted and measured temperature profiles. Temperatures predictions for locations 1 and 3 match very well the measured temperatures for the entire duration of the hydriding reaction. At location 2, the temperature is underpredicted initially and overpredicted towards the later part of the reaction. The predictions for location 4 compare well with experiment except for the

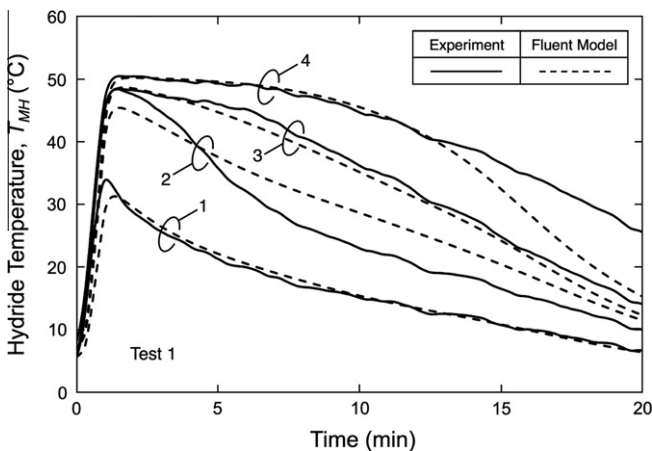


Fig. 4. Comparison of model predictions of hydride temperature response with experimental data from test 1.

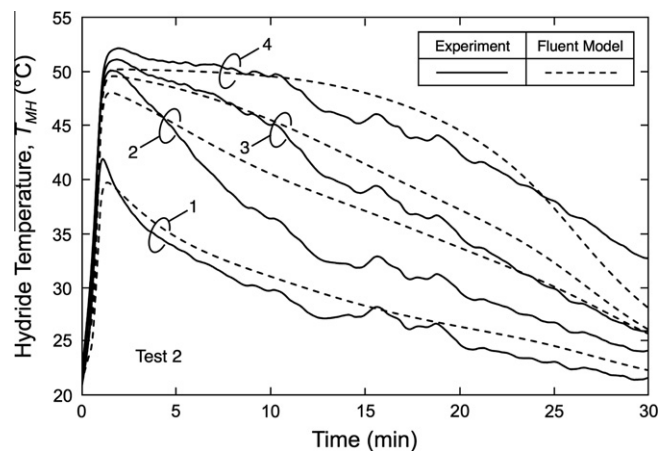


Fig. 5. Comparison of model predictions of hydride temperature response with experimental data from test 2.

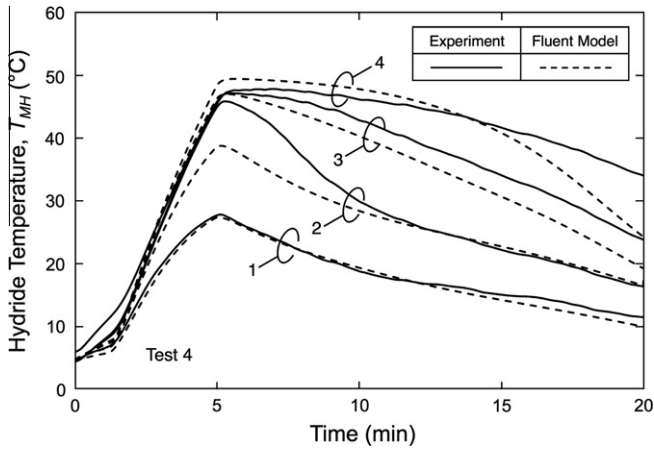


Fig. 6. Comparison of model predictions of hydride temperature response with experimental data from test 4.

end of the reaction, where the model predicts faster decay compared to the data.

There are a couple of possible reasons for the differences between the predicted and measured profiles, especially for location 2. First, movement of the hydride powder during filling and testing can cause local powder density to be different from the storage vessel average value used in the model (2.2 g/cc). Second, a thermocouple may shift slightly from the intended location during filling and testing, changing its distance from the coolant tube and measuring a profile slightly different from that of the intended location.

For location 4, which is farthest from the coolant tube, the faster decay predicted by the model can be explained by the metal hydride property assumptions. The model assumes a constant value of $c_{p,MH} = 750 \text{ J/kg K}$ throughout the hydriding reaction. However, as shown in Fig. 2, $c_{p,MH}$ increases to around 1000 J/kg K towards the end of the reaction. Use of a lower $c_{p,MH}$ value in the model compared to actual towards the end of the reaction causes the model to predict a faster temperature drop. However, the increased $c_{p,MH}$ value is far less important to the other locations, which are all closer to the coolant tube than location 4, because their temperatures are already close to coolant temperature by the time they reach the end of their reaction.

Fig. 7 compares the predicted average reaction progress, F_{avg} , for tests 1, 2 and 4, which is defined as

$$F_{avg} = \frac{\sum F_i v_i}{\sum v_i}, \tag{6}$$

where v_i is the volume of each computation cell and F_i the reaction progress for metal hydride contained in that cell. Thus, a value of $F_{avg} = 0.7$ indicates that the metal hydride bed on average has completed 70% of the reaction, although some locations may have completed more, while others less than 70%. A fill time, defined as the time needed to reach 90% completion ($F = 0.9$) of the hydriding reaction, is also indicated for each test. It can be seen from the plot that hydriding rate (slope of the curve) for each of the three tests is at its peak just at the end of the pressurization ramp (at 60 s for tests 1 and 2, and 300 s for test 4). Test 1, where the coolant temperature is lowest, achieved the shortest fill time of 12.2 min. Increasing the coolant temperature from 2.5 °C in test 1 to 21 °C in test 2 increases the fill time to 20.9 min. For test 4, which employed a slow 300 s long pressurization ramp but a coolant temperature close to that of test 1, achieved a fill time of 14.8 min, only slightly longer than for test 1. This proves that decreasing coolant temperature is most effective at reducing fill time than increasing pressurization rate.

While not calculated from the model, the fill time for test 3, with no coolant supplied through the tube, is estimated from the experimental data at about 40 min. This very long fill time demonstrates the importance of the heat exchanger to the hydrogen storage system.

4. Spatial distribution predictions

The computational model complements the experimental study by providing a detailed depiction of the spatial variations of key heat exchanger performance parameters during the hydriding reaction. Fig. 8(a), (b) and (c) show color spatial distribution contour plots of metal hydride temperature, T_{MH} , reaction progress, F , and volumetric heat generation rate, q''' , at different times during the hydriding process for test 1. Similar plots are shown in Figs. 9 and 10 for tests 2 and 4, respectively. For each time indicated, results are shown for two sections of the computational domain. The circular color plot to the left corresponds to a section along the axial center of the domain, perpendicular to the central straight portion of the coolant tube and parallel to the adiabatic surfaces. The rectangular plot to the right is for a vertical section along the center of the domain, parallel to the central portion of the coolant tube and perpendicular to the adiabatic surfaces. White regions in the plots correspond to the coolant tube.

Fig. 8(a) shows the spatial contour plots of metal hydride temperature over time for test 1. Time $t = 0$ corresponds to the onset of the pressurization ramp, and $t = 60 \text{ s}$ the end of the ramp. The metal hydride temperature increases as a result of heat generated due to both pressurization heating and hydriding reaction, the latter being the most dominant. Peak temperatures are reached within a short time (about 10 s) after the completion of the pressurization ramp. While the metal hydride reacts with the hydrogen and its temperature increases because of the heat released, it is simultaneously being cooled by the coiled heat exchanger. As depicted in Fig. 8(a) metal hydride particles located closest to the coolant tube cool faster, and are therefore the earliest to finish hydriding, while particles nearly halfway between the central tube and the coil cool the slowest. Notice how a ring of high temperature metal hydride persisting until about $t = 800 \text{ s}$; this region continues hydriding as powder in the rest had already finished hydriding. Similar temperature trends are observed in Fig. 9(a) for test 2 and Fig. 10(a) for test 4. Note that the temperature scale in Fig. 9(a) ranges from 20 to 55 °C as opposed to 0 to 55 °C in Figs. 8(a) and 10(a), due to the higher coolant temperature in test 2. Warmer

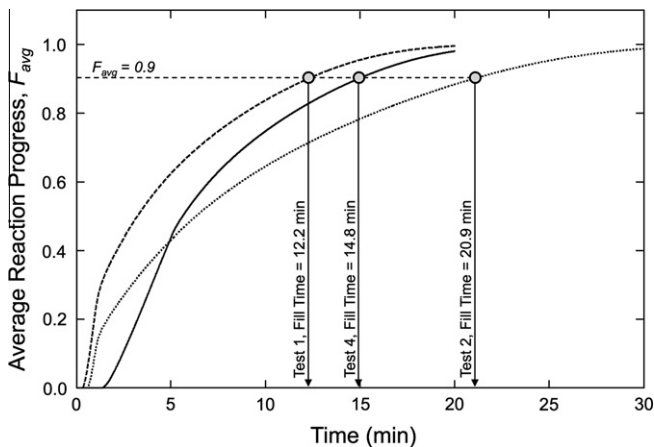


Fig. 7. Predicted reaction progress and fill times for tests 1, 2 and 4. For comparison, fill time for test 3 is estimated from measurements at 40 min.

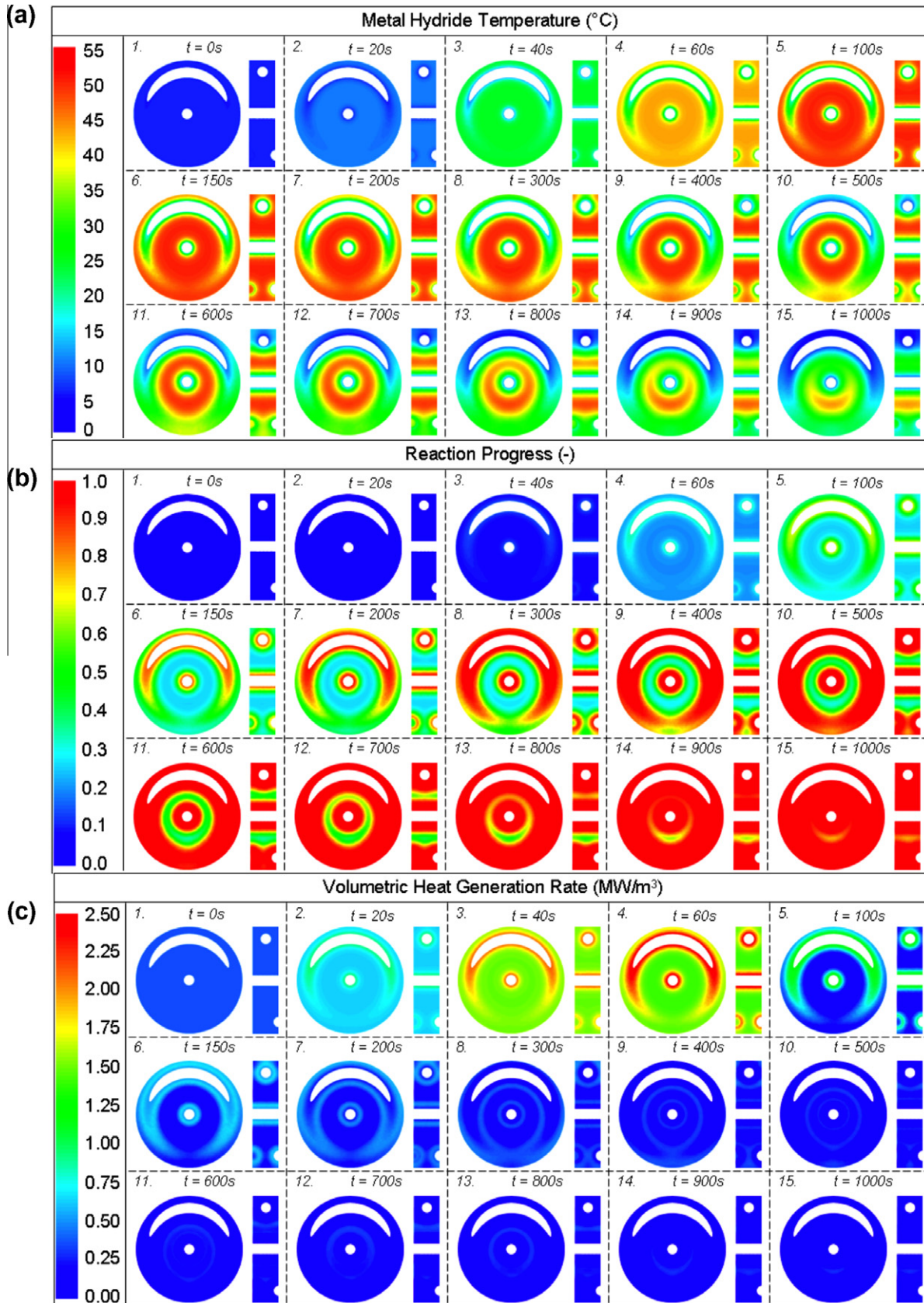


Fig. 8. Spatial distribution plots of predicted (a) hydride temperature, (b) reaction progress, and (c) volumetric heat generation rate at different times during the hydriding reaction for test 1.

coolant in test 2 (21 °C) decreases heat removal rate resulting in metal hydride particles closer to the coolant tube staying warmer

for a longer time, and the reaction rate decreasing. By comparing Figs. 8(a) and 9(a) at 300 s, it can be seen that, in test 1, more metal

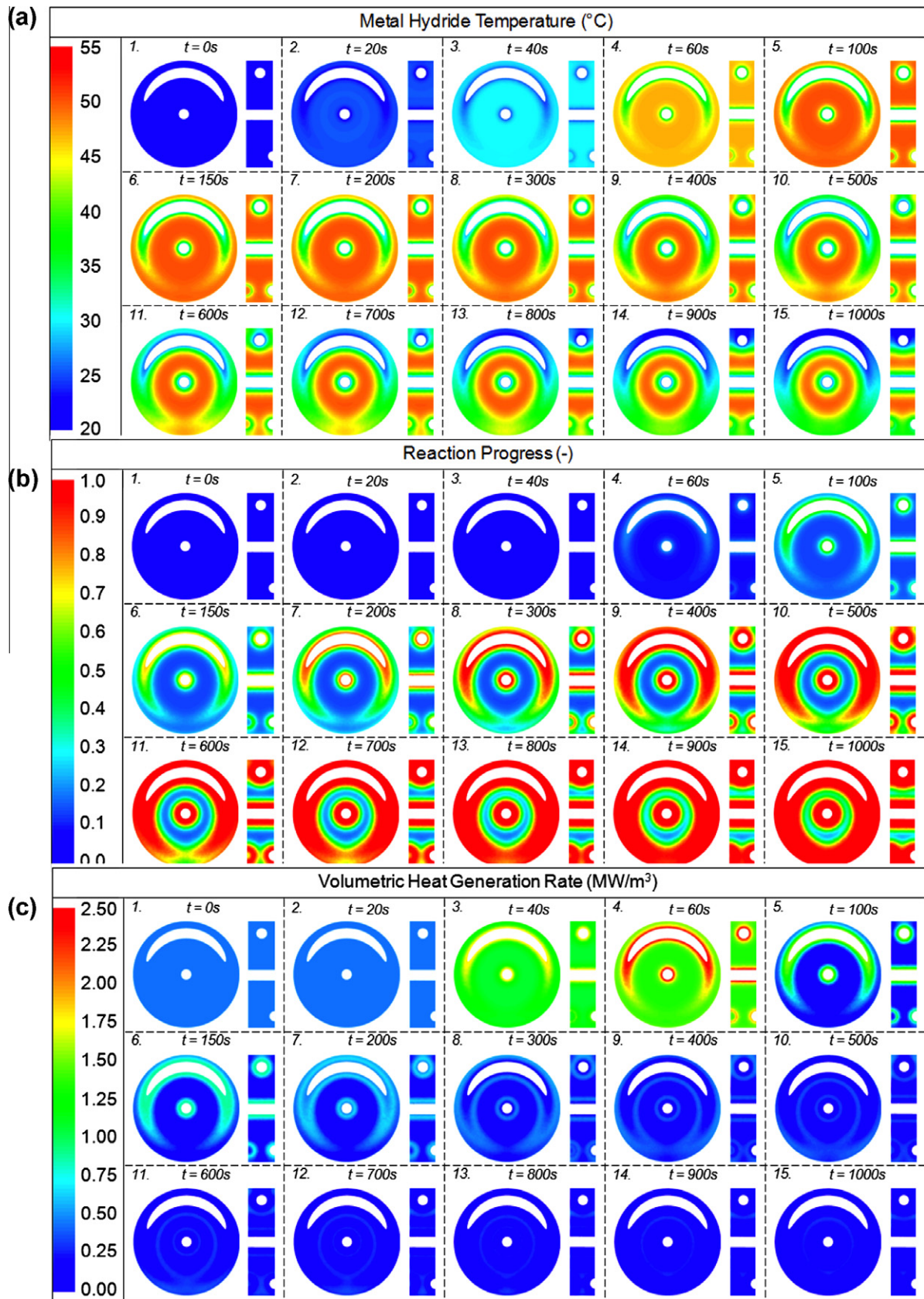


Fig. 9. Spatial distribution plots of predicted (a) hydride temperature, (b) reaction progress, and (c) volumetric heat generation rate at different times during the hydriding reaction for test 2.

hydride particles closer to the coolant tube have cooled and completed the reaction compared to those in test 2. Another inter-

esting observation is that, despite the much lower coolant temperature in test 1 ($2.5\text{ }^{\circ}\text{C}$), the metal hydride particles along the central

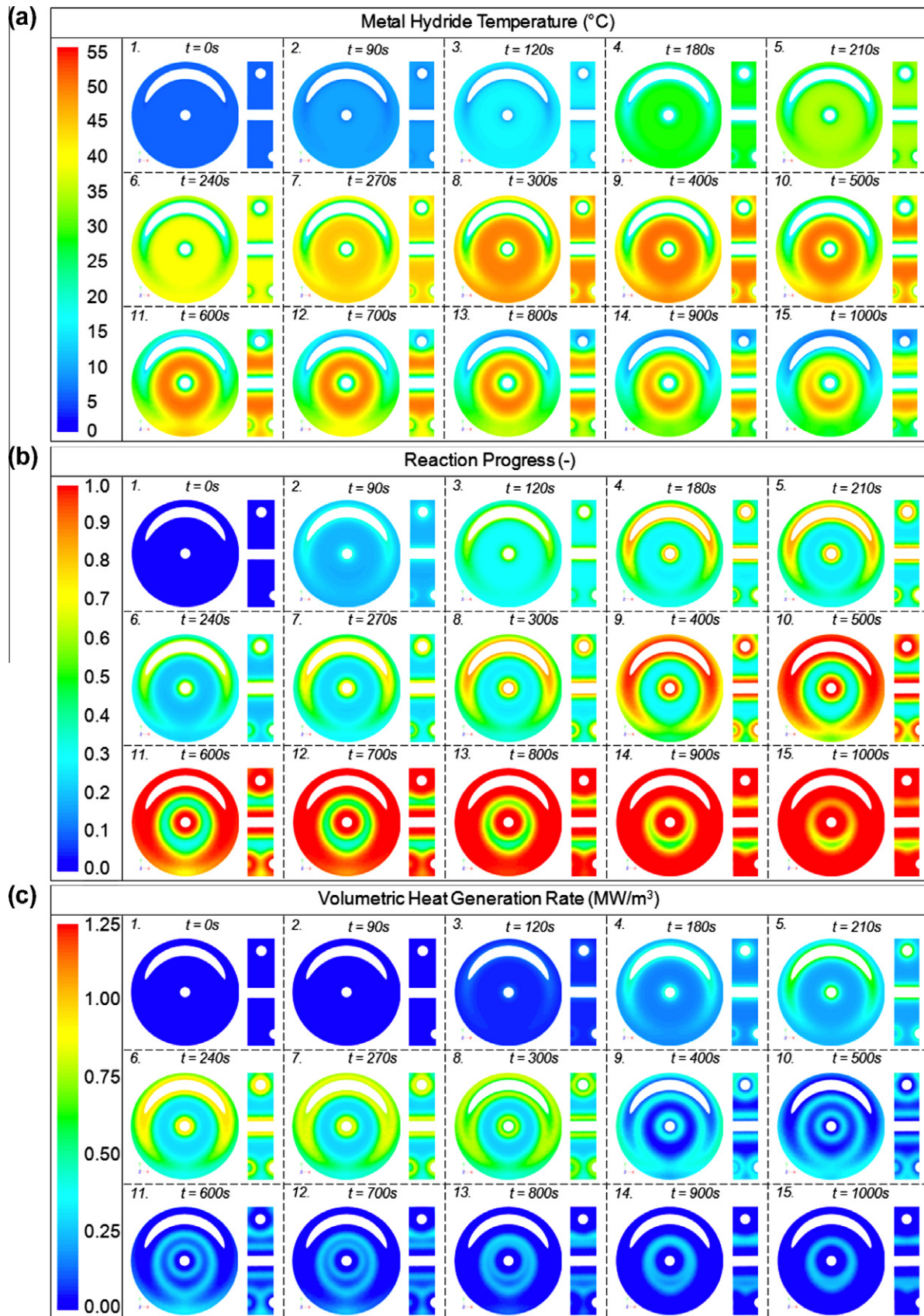


Fig. 10. Spatial distribution plots of predicted (a) hydride temperature, (b) reaction progress, and (c) volumetric heat generation rate at different times during the hydriding reaction for test 4.

ring are a few degrees warmer than in test 2. This can be explained by the fact that low coolant temperature in test 1 allows the metal hydride to react faster, thereby releasing greater amounts of heat. In test 4, due to the slower pressurization rate and therefore slower reaction rate, temperatures across the hydride bed are more uniform compared to tests 1 and 2. The peak hydride temperature reached during test 4 is around 47 °C, 4 to 5 °C lower than in tests 1 and 2.

Figs. 8(b), 9(b) and 10(b) show spatial contour plots of reaction progress for tests 1, 2 and 4, respectively. The reaction commences at hydride locations closest to the coolant tube. At 300 s in Fig. 8(b), the hydride particles surrounding the coolant tube have finished hydrating while particles in the central warm ring are just starting to react. In test 1, more than 90% of the hydride completes the reaction by 800 s. However, for test 2, high coolant temperature delays the reaction considerably, evidenced by the central region completing only 50% after 1000 s, when 80% of the hydride has finished reacting. Because of close coolant temperatures, tests 1 and 4 approach completion around similar times, with test 4 delayed by a couple of minutes due to the slightly warmer coolant and slow pressurization profile. The largest spatial variations of reaction progress are observed in test 2. Fig. 9(b) shows that, even after 800 s, there are particles in the central ring that have finished less than 10% of the reaction, while a substantial portion of the metal hydride bed had already completed reacting. This demonstrates that, with the high coolant temperature in test 2 (21 °C), the heat exchanger is unable to provide sufficient cooling to the hydride particles in the central ring, causing the reaction to virtually stall in that region until the particles everywhere else have finished hydrating. On the other hand, lower coolant temperature provides better temperature uniformity for tests 1 and 4, where, at 600 s, when most of the hydride particles outside the central ring have finished reacting, the particles in the ring are at 40% to 50% reaction progress.

Figs. 8(c), 9(c) and 10(c) show spatial contour plots of volumetric heat generation rate for tests 1, 2 and 4, respectively. Fast pressurization causes tests 1 and 2 to achieve peak heat generation rates of 2.5 MW/m³ at the end of the pressure ramp (60 s). Within a couple of minutes thereafter, the peak heat generation rate drops in both tests below 1 MW/m³ because of the slowing reaction rate. In test 4, due to slower pressurization rate and more uniform hydrating, the peak heat generation rate is less than 1.25 MW/m³. At 20 s in test 1, metal hydride particles have already started reacting due to lower initial and coolant temperatures. However in tests 2 and 4, the hydride particles have not yet started hydrating because of higher initial and coolant temperatures, and slower pressurization rate, respectively. Comparing Figs. 8(c) and 9(c) at 40 s shows that the lower coolant temperature in test 1 causes metal hydride particles near the coolant tube to hydrate at a very fast rate, momentarily releasing more than 2.25 MW/m³ of heat, while, in test 2, particles at the same locations are releasing a smaller heat rate of about 1.75 MW/m³. Also, at subsequent times, the spread in heat generation rate is always greater in test 1 than in test 2. Fig. 10(c) shows that the hydride particles in test 4 start reacting at 120 s, when the vessel pressure exceeds the equilibrium pressure corresponding to the metal hydride temperature. At 240 s, hydride particles within a thin layer along the surface of the coolant reach the peak heat generation rate of about 1.25 MW/m³. The striking differences in hydrating pattern among tests 1, 2 and 4 are quite apparent when comparing Figs. 8(c), 9(c) and 10(c). At any instant during the hydrating reaction, there are fewer particles that are reacting in tests 1 and 2 compared to test 4. However, the hydrating particles in tests 1 and 2 are doing so at faster rate, releasing larger amounts of heat in a more localized manner than in test 4. The reaction in test 4 is spatially more uniform.

5. Conclusions

This paper presented a 3D computational model of a high-pressure metal hydride (HPMH) hydrogen storage system that is cooled by a coiled-tube heat exchanger. A representative computational domain of the hydride powder was defined and appropriate initial and boundary conditions applied. The model is used to track both spatial and temporal variations of the heat exchanger's key performance parameters during the hydrating process resulting from reaction of the hydrogen with the hydride powder. The model predictions are compared to experimental results presented in the first part of this two-part study. Key conclusions from the study are as follow.

1. The 3D model shows good agreement with hydride temperatures measured at four representative locations within the hydride powder. Sources of disagreement between the model predictions and measurements include spatial variations of hydride density, slight shifting of thermocouples from intended locations, and variations of the hydride's specific heat towards the end of hydrating reaction.
2. Coolant temperature has an appreciable influence on fill time. The model predicts an increase in the fill time from 12.2 to 20.9 min when the coolant temperature is increased from 2.5 to 21 °C. Slow pressurization, on the other hand, has a far weaker effect of fill time. The fill time predictions agree well with the reaction time measured from the hydrogen flow rates during the experiments.
3. Spatial color contour plots constitute an effective means for tracking the detailed variations of hydride temperature, reaction progress and volumetric heat generation rate for different locations relative to the coolant tube during the hydrating process. The hydrating reaction commences at locations closest to the coolant tube and eventually propagates towards warmer locations away from the coolant tube. Metal hydride particles located closest to the coolant tube also finish hydrating the earliest. Heat generation rate is highest just at the end of the pressurization ramp when the hydrating reaches peak reaction rate. The hydrating reaction is spatially more uniform when it is kinetically limited (vessel pressure below equilibrium pressure, as encountered in test 4). Conversely, when the reaction is thermally limited due to insufficient cooling (test 2), the hydrating tends to be more localized with high local reaction and heat release rates and large spatial temperature gradients within the hydride bed. Overall, understating these spatial variations can aid in determining optimum placement of the coolant tube relative the hydride powder.

References

- [1] D. Mori, K. Hirose, Recent challenges of hydrogen storage technologies for fuel cell vehicles, *Int. J. Hydrogen Energy* 34 (2009) 4569–4574.
- [2] T. Pourpoint, V. Velagapudi, I. Mudawar, Y. Zheng, T. Fisher, Active cooling of a metal hydride system for hydrogen storage, *Int. J. Heat Mass Transfer* 53 (2010) 1326–1332.
- [3] M. Visaria, I. Mudawar, T. Pourpoint, Enhanced heat exchanger design for hydrogen storage using high-pressure metal hydride – part 1. Design methodology and computational design, *International Journal of Heat and Mass Transfer* 54 (2011) 413–423.
- [4] M. Visaria, I. Mudawar, T. Pourpoint, Enhanced heat exchanger design for hydrogen storage using high-pressure metal hydride – part 2. Experimental results, *Int. J. Heat Mass Transfer* 54 (2011) 424–432.
- [5] M. Visaria, I. Mudawar, Coiled-tube heat exchanger for high-pressure metal hydride hydrogen storage systems – part 1. Experimental study, *Int. J. Heat Mass Transfer* 54 (2011) 424–432.
- [6] P. Goodell, P. Rudman, Hydrating and dehydrating rates of the LaNi₅-H system, *J. Less Common Metals* 89 (1983) 117–125.
- [7] S. Suda, N. Kobayashi, K. Yoshida, Reaction kinetics of metal hydrides and their mixtures, *J. Less Common Metals* 73 (1980) 119–126.

- [8] S. Mellouli, F. Askri, H. Dhaou, A. Jemni, S. Ben Nasrallah, Numerical simulation of heat and mass transfer in metal hydride hydrogen storage tanks for fuel cell vehicles, *Int. J. Hydrogen Energy* 35 (2010) 1693–1705.
- [9] C. Chung, Ci-Jyun Ho, Thermal-fluid behavior of the hydriding and dehydriding processes in a metal hydride hydrogen storage canister, *Int. J. Hydrogen Energy* 34 (2009) 4351–4364.
- [10] T. Forde, E. Naess, V.A. Yartys, Modelling and experimental results of heat transfer in a metal hydride store during hydrogen charge and discharge, *Int. J. Hydrogen Energy* 34 (2008) 5121–5130.
- [11] A. Jemni, S. Ben Nasrallah, Study of two-dimensional heat and mass transfer during desorption in a metal-hydrogen reactor, *Int. J. Hydrogen Energy* 20 (1995) 881–891.
- [12] U. Mayer, M. Groll, W. Supper, Heat and mass transfer in metal hydride reaction beds: Experimental and theoretical results, *J. Less Common Metals* 131 (1987) 235–244.
- [13] K. Aldas, M. Mat, Y. Kaplan, A three-dimensional mathematical model for absorption in a metal hydride bed, *Int. J. Hydrogen Energy* 27 (2002) 1049–1056.
- [14] M. Visaria, I. Mudawar, T. Pourpoint, S. Kumar, Parametric study of heat transfer and kinetics parameters influencing the design of heat exchangers for hydrogen storage in high-pressure metal hydrides, *Int. J. Heat Mass Transfer* 53 (2010) 2229–2239.
- [15] S. Flueckiger, T. Voskuilen, T. Pourpoint, T.S. Fisher, Y. Zheng, In situ characterization of metal hydride thermal transport properties, *Int. J. Hydrogen Energy* 35 (2010) 614–621.
- [16] T. Voskuilen, Y. Zheng, T. Pourpoint, Analysis of the hydrogen sorption kinetics of $Ti_{1.1}CrMn$, paper no. AIAA-2009-4502, in: 7th International Energy Conversion Engineering Conference, Denver, CO, 2009.